Effect of Ceria on the organization and bio-ability of anatase fullerene-like crystals

Noel Gravina[a], Juan M. Ruso[b], Doris A. Mbeh[c], L'Hocine Yahia[c], Yahye Merhi[d], Javier Sartuqui[a], Paula V. Messina[a]*

(a) Department of Chemistry, Universidad Nacional del Sur, 8000, Bahía Blanca, Argentina. INQUISUR-CONICET. (b) Soft Matter and Molecular Biophysics Group, Department of Applied Physics, University of Santiago de Compostela, Santiago de Compostela, 15782, Spain. (c) Laboratory for Innovation and Analysis of Bio-Performance, École Polytechnique de Montréal, C.P. 5079, Succursale Centre-Ville Montréal, Quebec, Canada H3C 3A7. (d) Montreal Heart Institute & Université de Montréal, 5000 rue Belanger, Montréal, Quebec, Canada H1T 1C8.

[*] Author to whom correspondence should be addressed. Department of Chemistry, Universidad Nacional del Sur, 8000, Bahía Blanca, Argentina. INQUISUR-CONICET. Tel: +54 291 4595159. Fax: +54 291 4595160. Electronic mail: pmessina@uns.edu.ar.

Descriptions of selected synthesis condition steps and their effect on the final material structures:

Effect of microemulsion conditions
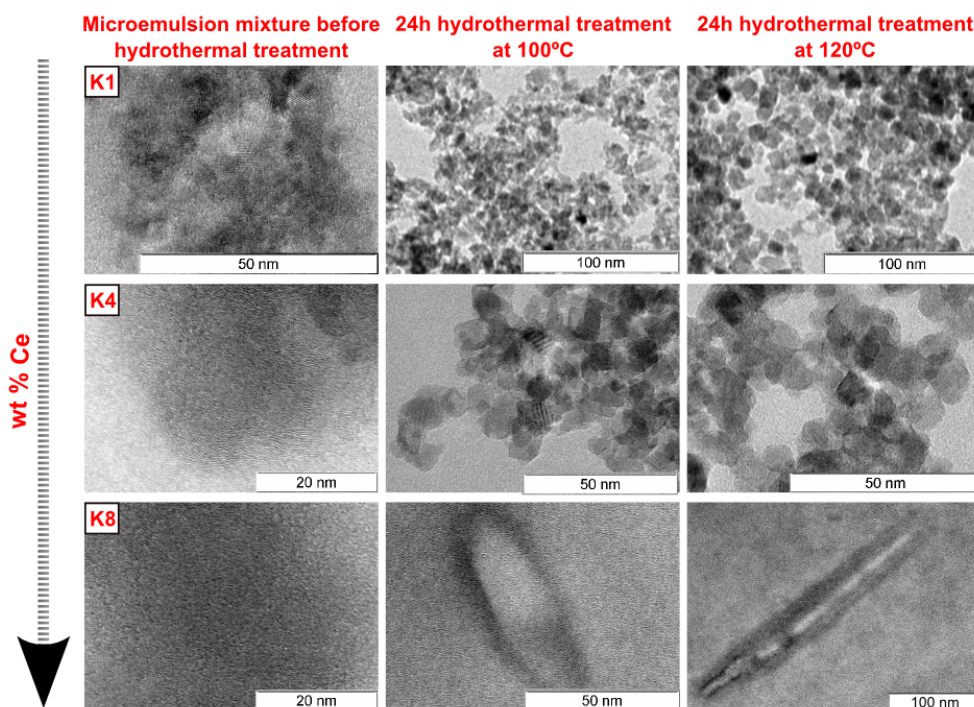
ESI1: H-TEM temperature evolution under hydrothermal treatment of **(a)** 0, **(b)** 6.0×10^{-3}, **(h)** 0.30 Ce(Val)$_3$/ TTIP molar ratio fullerene-like structures.

Figure ESI1 shows the H-TEM of representative samples, K1, K4 and K8 (wt% Ce increase), at different steps of the synthetic route. It can be seen that a multitude of crystalline planes folding in all directions appeared from the beginning of the process indicating that the inorganic fullerene-like (IF) structure formation initiated at the microemulsion stage. Therefore, the dynamic nature of the reverse microemulsion droplet exerts a key role in the formation of Ce-TiO$_2$ fullerene-like structures. The formation of IF structures involves a high elastic strain[1], that in turn, can be correlated to the rigidity of the nano-droplet in the oil-water interface. In previous studies [2-5] we assessed the effect of interfacial micro-droplet rigidity on the final nano-material morphology and the crystalline microstructure. The hydrolyses of titanium alkoxides are very complex[6]; these reactions produce polycondensates which chemical compositions are a function of their physical size and polymeric morphology. For TTIP hydrolysis[7], it was found that the reaction occurred via an associative mechanism and it was detected an intermediary with a coordination number of five –

OR groups. Microemulsion systems have been prepared with water/Ti^{4+} and oil/Ti^{4+} molar ratio values of about 10; those which are between 4 and 17 times larger than Ti^{4+}/surfactant ratio in all samples, see **table 1**. Under these experimental conditions, there is a fast diffusion of Ti^{4+} ions through continuous organic phase inside the aqueous microemulsion droplets and a fast hydrolysis of TTIP in comparison with the microemulsion inter-droplet exchange rate[8]. The oxide network extends as far as the hydrolysis conditions permit[6] limited by microemulsion confinements and related to micro droplet interfacial elasticity.

Table 1. Ce-doped anatase IFS synthesis conditions.

| Sample | Microemulsion "A" | | | | | Solution "B" | | Final microemulsion conditions | | | | |
	wt% CTAB	wt% ButOH	wt% water	%wt oil	%wt Ce(Val)$_3$	wt% oil	wt% TTIP	S_0	W_0	TTIP / CTAB	ButOH / CTAB	Ce(Val)$_3$ / TTIP
K1	9.68	47.06	9.68	33.68		63.4	36.6	25.3	20.1	2.5	24	
K2	9.68	47.05	9.68	33.57	0.02	63.4	36.6	25.3	20.1	2.5	24	6.0×10^{-4}
K3	9.68	47.05	9.68	33.57	0.02	78.3	21.7	25.3	20.1	1.2	24	1.2×10^{-3}
K4	9.67	47.02	9.67	33.55	0.09	78.3	21.7	25.3	20.1	1.2	24	6.0×10^{-3}
K5	9.66	46.98	9.66	33.53	0.17	78.3	21.7	25.3	20.1	1.2	24	0.012
K6	9.60	46.65	9.60	33.29	0.86	78.3	21.7	25.3	20.1	1.2	24	0.06
K7	9.52	46.25	9.52	33.00	1.71	78.3	21.7	25.3	20.1	1.2	24	0.12
K8	9.48	46.05	9.48	32.86	2.13	87.8	12.2	25.3	20.1	0.6	24	0.30

An alternative mechanism for the growth of crystalline curved structures may involve the participation of contaminant atoms in the crystal lattice[9]. To elucidate this, we have taken into account that during the synthetic process of IF structures Ce atoms were added to TiO_2 matrix. It is possible that the presence of Ce(Val)$_3$ bulkier groups in the material synthesis has several concurrent effects. On one hand, it influences the interfacial organization by affecting the compactness of the surfactant film and its temporal stability. It might also modify the packing parameter and, in turn, manipulate the radius of curvature of the microemulsion droplet in a way that causes an increase of the oil-water interface stiffness. If the molecules are allowed to adjust their area per molecule depending on the curvature, the interface will be less rigid upon bending resulting in elongated structures. Similar effects were observed during the preparation of Ce-doped SiO_2 and Ce-doped TiO_2 materials[4, 5] by an analogous procedure. Otherwise, the existence of Ce atom contaminants possibly reduces or eliminates the strain of bending of TiO_2 layers through the formation of cerium oxide structures at the corners. Both effects lead to the growth of fullerene-like structures dropped from nanoparticles to multi-wall elongated structures.

Effect of hydrothermal and annealing conditions

Figure ESI1 also shows the temperature evolution of IF structures under hydrothermal treatment. At any tested temperature, the observed material maintain the multi-wall onion-like morphologies. However, it can be noted a different effect on sample organization with respect to the Ce content.

For sample K1 (pure TiO$_2$ material), hydrothermal treatment caused a segregation of the microemulsion mixture and the formation of undefined structures where it can be observed isolated particles with slightly some kind of polyhedral shape. The augment of wt% Ce in the materials induced the formation of elongated structures, as we discussed in the above section. Essentially, there are two mechanism proposed for the microemulsion mediated synthesis of inorganic nanowires/nanorods: the template-directed growth and the oriented aggregations[8]. In the template-directed growth mechanism, elongated water droplets or interconnected water channels play the role of template to induce the formation of elongated nuclei, which finally grow into nanorods with dimensions considerably larger than the templates. In the oriented aggregation mechanism, precipitation within spherical water droplets initially results in the formation of surfactant-encapsulated primary nanoparticles which subsequently undergo oriented aggregation involving linear attachment and coalescence owing to specific interactions of inorganic crystals with surfactants leading to the growth of single-crystalline nano-wires. Under hydrothermal conditions, an oriented aggregation mechanism is usually adopted because reverse micelles may be destroyed under synthesis conditions[8]. When the film is highly flexible, this is not the case, by subjecting the microemulsion to the effect of the hydrothermal treatment, reverse micelles brake as shown in the oriented aggregation mechanism[8] and due to their elastic interface, the nano-droplets merge adopting a bicontinuous structure[2, 4, 5]. As a result, the final obtained material showed a non-defined or a bicontinuous structure. In contrast, if the film is highly inflexible the formation of small structured particles takes place: samples K1-K4. When the film seems to be flexible enough, the configuration of interconnected channels is avoided and the inorganic material growing inside the droplets lead to the formation of lengthened structures whose expansion are limited to interfacial elasticity: samples K5-K8. **Figure ESI2** shows the diffraction patterns of the structures at different points of the synthesis. It can be seen that before hydrothermal treatment samples K1, K4 and K8 show DRX patterns of amorphous materials. The sample K8 remains with an amorphous appearance after hydrothermal treatment regardless of the applied temperature. H-TEM analysis of the same samples, **figure ESI1**, indicated that crystalline planes are present from the beginning of the synthesis. Being bent, the crystalline planes induce a poor crystallized appearance into the DRX pattern and it was not possible to assign defined diffraction peaks. Crystalline peaks associated to pure anatase structures can be appreciated from the DRX of K1 and K4 samples analyzed after the hydrothermal stage. No traces of diffraction peaks due to cerium oxide or other TiO$_2$ structures were detected. During isothermal hydrothermal heating, as in our synthesis procedure, the temperature quickly jumps to a certain value and remains constant. Consequently, the larger fraction of the titania condensation or hydrolysis occurs at high temperatures, causing a growth in

the crystallinity of the material. The effect of Ce atom on the crystalline structure was partially analyzed in the precedent section demonstrating that results in poor titania-titania connectivity; favoring the formation of fullerene-like structures and supporting the theory that Ce contaminating atoms play a key role in their generation.
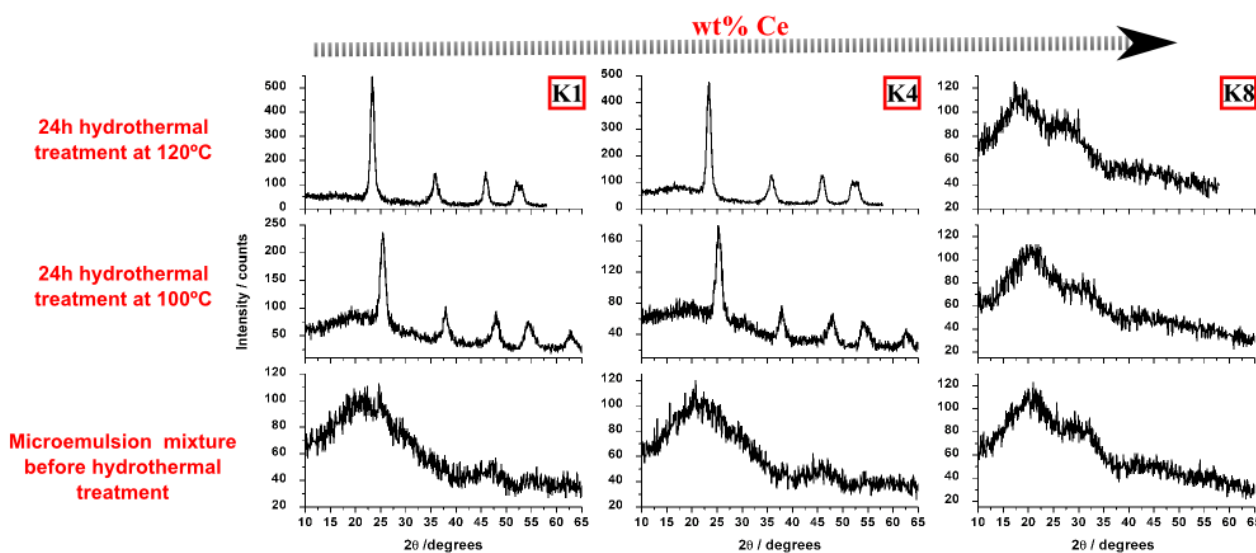
ESI2. Crystallinity temperature evolution under hydrothermal treatment of **(a)** 0, **(b)** 6.0×10^{-3}, **(h)** 0.30 Ce(Val)$_3$/ TTIP molar ratio fullerene-like structures.

Structural characterization:

X-ray energy dispersive (EDX) microanalysis indicates that the basic components of all the samples were Ti, Ce and O. The presence of Aluminium (Al) peak is due to the sample support, it intensity is specific of the material zone analyzed, i.e. more or less contact with the sample support. Nd and Ce elements are both simultaneously detected due to similarity in their characteristics X-ray dispersive energies.
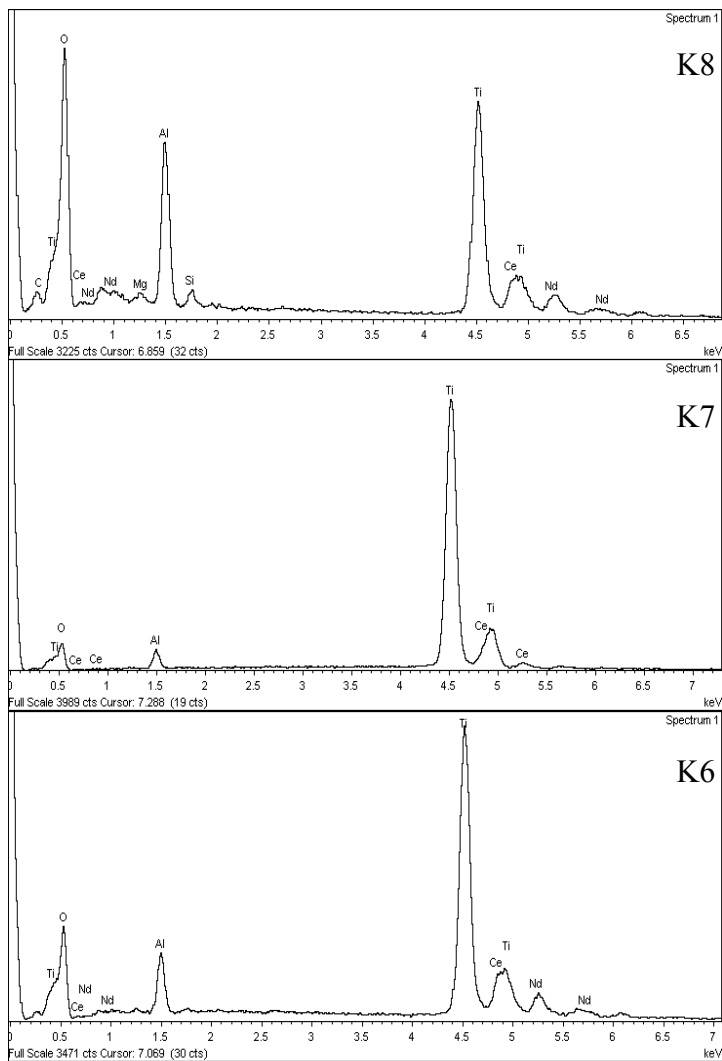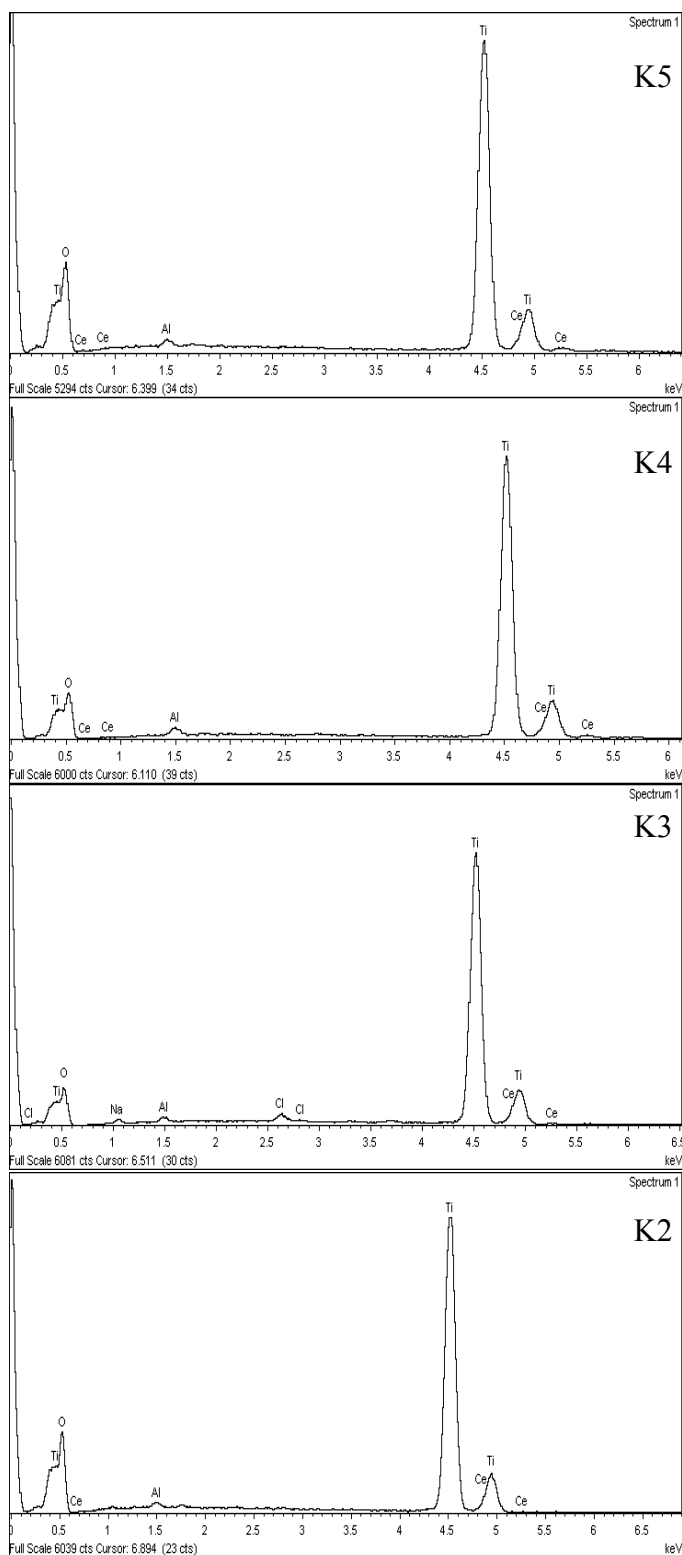
ESI3. X-ray energy dispersive (EDX) microanalysis

Representative distribution size histograms, a similar analysis were performed with all samples.

K1
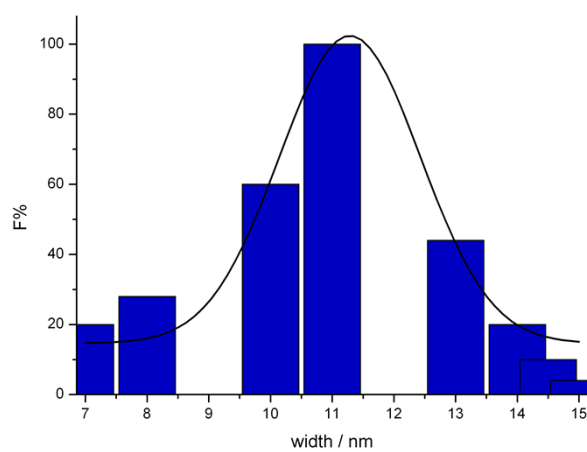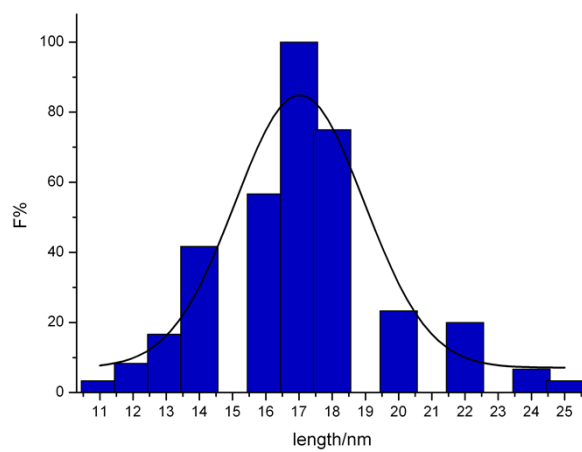
K4
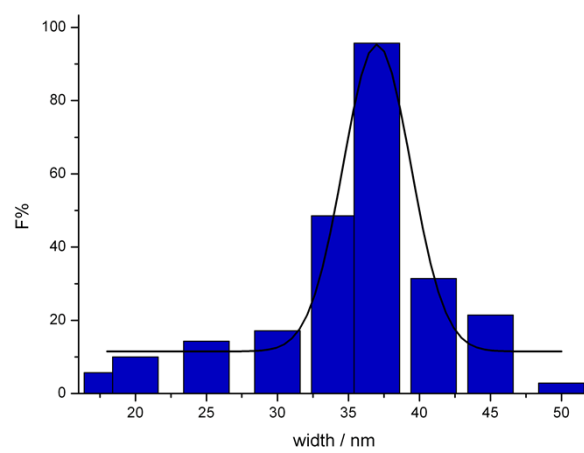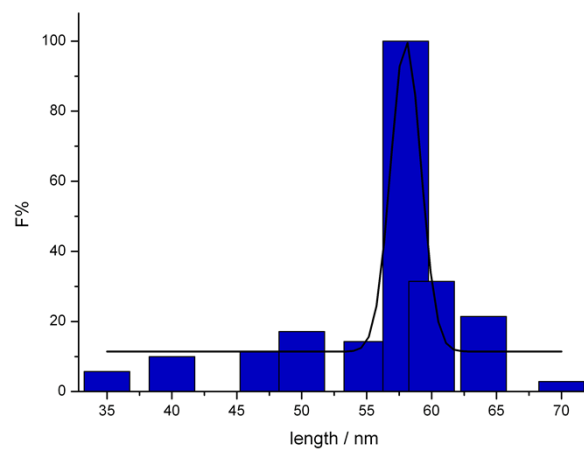
ESI4. Representative distribution size histograms

Parameters for calculation and comparison of powder diffraction pattern:

The neutron and x-ray diffraction of powder samples results in a pattern characterised by reflections (peaks in intensity) at certain positions. The height, width and position of these reflections can be used to determine many aspects of the materials structure. For this purpose the Rietveld refinement method is used.[10] [11]

Theoretical regular anatase crystal
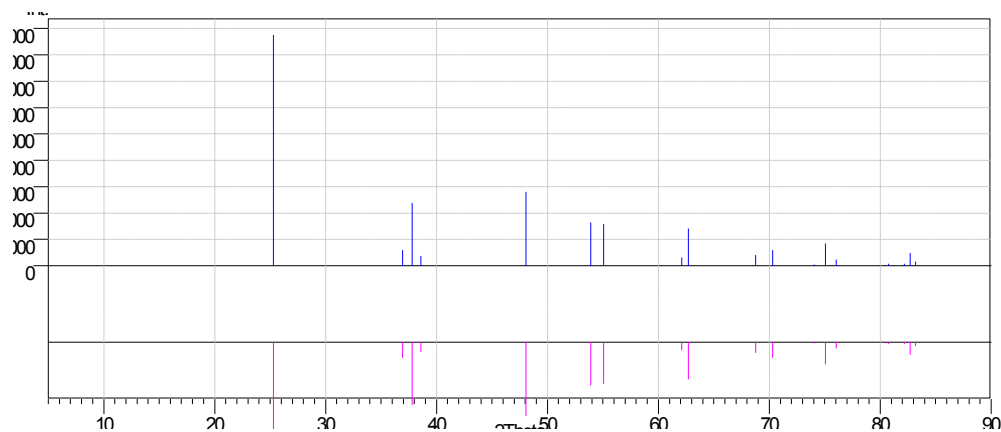
ESI5. Theoretical regular anatase crystal diffraction pattern

Comparison of K2 material with anatase crystal

```
Parameters used in optimization

Start value of random number simulator (seed)     1
Optimization speed (optspeed)     8
Pareto parameter for costfunction (alpha)         0.500000

Potential used for calculation of potential energy:

Coulomb interactions:    Ewald sum
Two-body potential:      simple repulsion

Parameters for repulsion potential:

Interaction       min. distance [Å]
 O(-2.0) -  O(-2.0)      2.400000
 O(-2.0) - Ti( 4.0)      1.950000
 O(-2.0) - Ce( 4.0)      2.350000
Ti( 4.0) - Ti( 4.0)      2.500000
Ti( 4.0) - Ce( 4.0)      3.100000
Ce( 4.0) - Ce( 4.0)      3.150000

Parameters for calculation and comparison of powder diffraction patterns:

Scattering:    X-ray
Scattering coefficients:

El       chrg    a1      b1      a2      b2      a3      b3      a4      b4      c
O        -2.0    4.75800 7.83100 3.63700 30.0500 0.00000 0.00000 0.00000 0.00000
1.59400
Ti       4.0     19.5114 0.17885 8.23473 6.67018 2.01341 -0.2926 1.52080 12.9464
-13.280
Ce       4.0     20.3235 2.65941 19.8186 0.21885 12.1233 15.7992 0.14458 62.2355
1.59180

Lorentz- and Polarization-correction are applied in intensity calculation.

Wavelength of radiation [Å]     1.540598
Geometry of diffractometer      Debye-Scherrer
Background intensity     0.100000
Minimum value of 2theta [°]     2.000000
Maximum value of 2theta [°]     80.737000

Terminate optimization when controlparameter falls below: tlimit= -999.000000

Local optimization:

Steps   % finished    costfunction    R-factor [%]
0       0             8901.795898     71.8
100     0             182.819504      67.9
200     0             146.171509      34.9
300     0             143.136276      31.4
400     0             143.059189      30.7
500     0             143.059189      30.7
600     0             143.038177      30.7
700     0             143.038177      30.7
800     0             143.038177      30.7
900     0             143.038177      30.7
1000    0             143.038177      30.7
1100    0             -84491.054688   69.0
1200    0             -84491.054688   69.0
1300    0             -84491.054688   69.0
1400    0             -84491.054688   69.0
1500    0             -84491.054688   69.0
1600    0             -84491.054688   69.0

1700    0             -84491.054688   69.0
1800    0             -84491.054688   69.0
1900    0             -84491.054688   69.0
2000    0             -84491.054688   69.0
2100    0             -84491.054688   69.0
2200    0             -84491.054688   69.0
2300    0
```

ESI6. Theoretical and experimental diffraction pattern of synthesized anatase crystal

The experimental and theoretical data match in a 95%.

Incorporation of Ce atom to anatase structure

```
Parameters used in optimization

Start value of random number simulator (seed)    1
Optimization speed (optspeed)     8
Pareto parameter for costfunction (alpha)       0.500000

Potential used for calculation of potential energy:

Coulomb interactions:    Ewald sum
Two-body potential:      simple repulsion

Parameters for repulsion potential:

Interaction      min. distance [Å]
 O(-2.0) -  O(-2.0)      2.400000
 O(-2.0) - Ti( 4.0)      1.950000
 O(-2.0) - Ce( 4.0)      2.350000
Ti( 4.0) - Ti( 4.0)      2.500000
Ti( 4.0) - Ce( 4.0)      3.100000
Ce( 4.0) - Ce( 4.0)      3.150000

Parameters for calculation and comparison of powder diffraction patterns:

Scattering:     X-ray
Scattering coefficients:

El       chrg    a1      b1      a2      b2      a3      b3      a4      b4       c
O        -2.0    4.75800 7.83100 3.63700 30.0500 0.00000 0.00000 0.00000 0.00000
1.59400
Ti        4.0    19.5114 0.17885 8.23473 6.67018 2.01341 -0.2926 1.52080 12.9464
-13.280
Ce        4.0    20.3235 2.65941 19.8186 0.21885 12.1233 15.7992 0.14458 62.2355
1.59180

Lorentz- and Polarization-correction are applied in intensity calculation.

Wavelength of radiation [Å]      1.540598
Geometry of diffractometer       Debye-Scherrer
Background intensity    0.100000
Minimum value of 2theta [°]      2.000000
Maximum value of 2theta [°]      80.737000

Terminate optimization when controlparameter falls below: tlimit= -999.000000

Local optimization:

Steps   % finished      costfunction    R-factor [%]
0       0               8901.795898      71.8
100     0               182.819504       67.9
200     0               146.171509       34.9
300     0               143.136276       31.4
400     0               143.059189       30.7
500     0               143.059189       30.7
600     0               143.038177       30.7
700     0               143.038177       30.7
800     0               143.038177       30.7
900     0               143.038177       30.7
1000    0               143.038177       30.7
1100    0              -84491.054688     69.0
1200    0              -84491.054688     69.0
1300    0              -84491.054688     69.0
1400    0              -84491.054688     69.0
1500    0              -84491.054688     69.0
1600    0              -84491.054688     69.0

1700    0              -84491.054688     69.0
1800    0              -84491.054688     69.0
1900    0              -84491.054688     69.0
2000    0              -84491.054688     69.0
2100    0              -84491.054688     69.0
2200    0              -84491.054688     69.0
2300    0
```

ESI7. Theoretical and experimental diffraction pattern of synthesized K2 material

The experimental and theoretical data match in a 90%.

Inter-atomic distances calculation in the anatase matrix

d_{Ti-O}^{eq}, d_{Ti-O}^{ap}, d_{O-O}^{eq}, d_{O-O}^{sh}, d_{O-O}^{ush} distances were computed considering $u = 0.208$ (regular anatase crystal) and the extreme planar condition with $u = 0.25$. The representation of both set of values versus the Ce / Ti molar ratio has the same tendency.

Ti-O apical distance
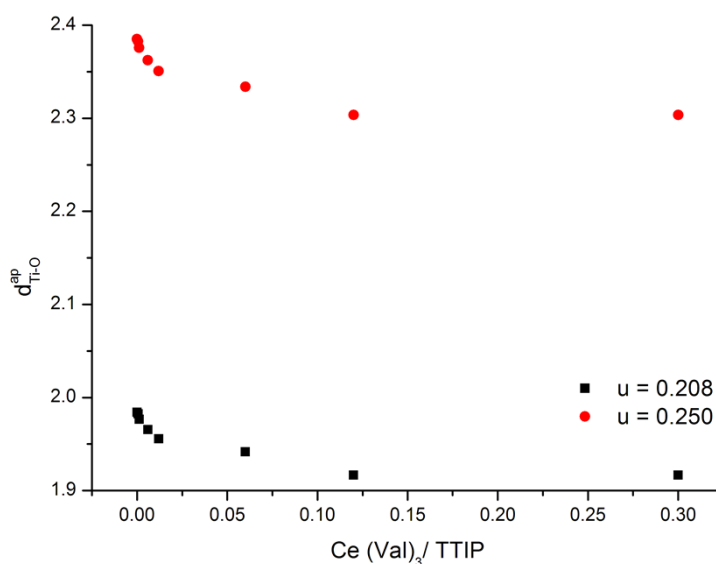
ESI 8. Ti-O apical distance

Ti-O equatorial distance
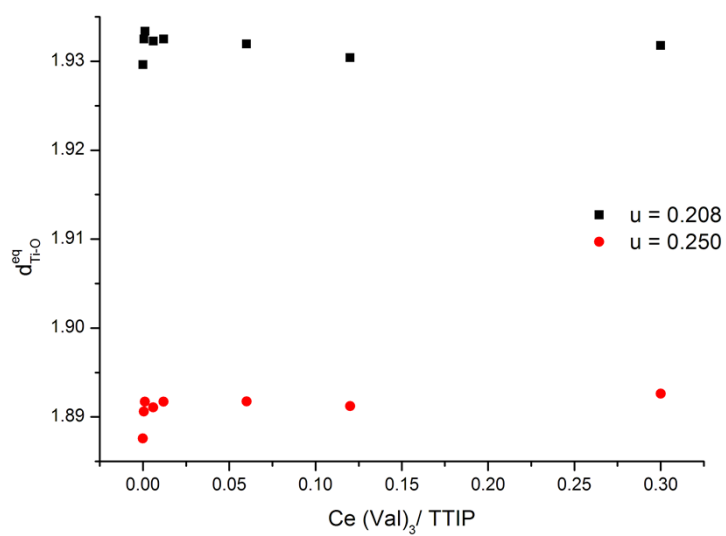
ESI 9. Ti-O equatorial distance

O-O equatorial distance
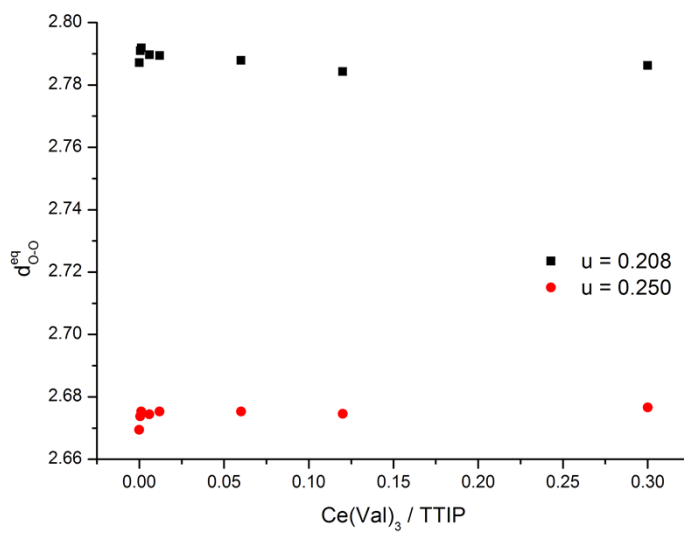
ESI10. O-O equatorial distance

Distance between an apical oxygen and an equatorial oxygen belonging to a shared edge
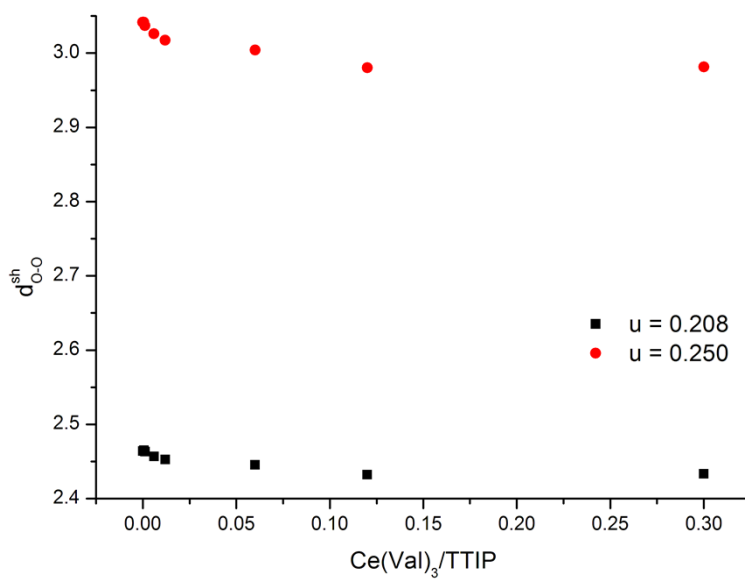
ESI11. Distance between an apical oxygen and an equatorial oxygen belonging to a shared edge

FT-Raman of doped and undoped materials
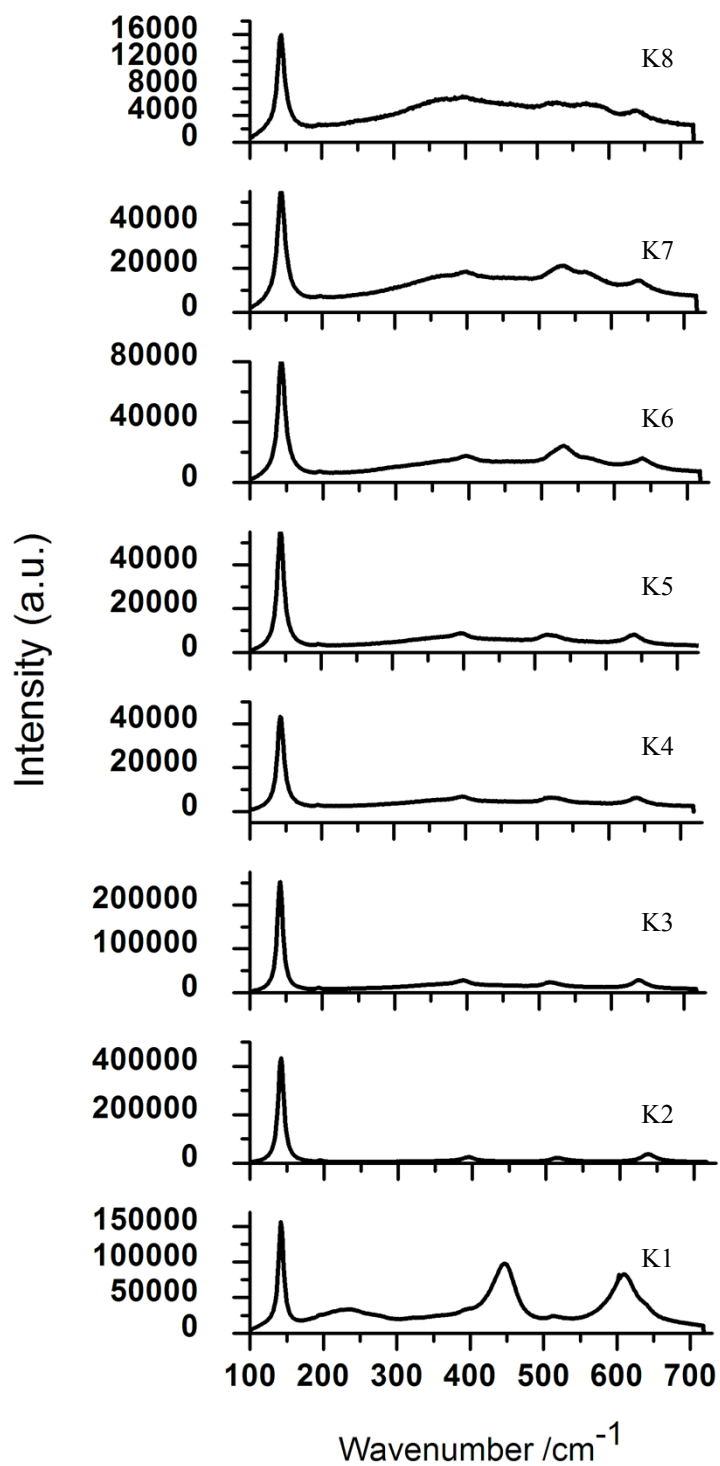
ESI12. Raman spectra of K1-K8 materials

Photoluminescence of doped and undoped materials

Fluorescence spectra were recorded at 25°C by a Varian Cary Eclipse spectrofluorometer under excitation by UV light at 220 nm, using a 1 cm path length quartz cell. The spectrum was obtained after the materials sonication in ethanol to yield homogeneous dispersions. Pure ethanol solution was used as black. Pure Anatase material shows two bands centered at 287 nm and at 370 nm. The peak at 287 nm is weak and can be attributed to a direct vertical transition of photo-induced electrons and holes in TiO_2. The peak at 370 nm is of high intensity and can be assigned to the band-to-band recombination because it is near-band-edge luminescence and/or to the exciton trapped at shallow-level defects[12]. The presence of Ce atom on anatase structure shows a noticeable effect on the photoluminescence band intensities. In all materials containing cerium the band centered at 287 nm disappeared while the intensity of the band peaked at 370 nm varied with the Ce/TTIP proportion. A representation of the Intensity% of the band peaked at 370 nm against the Ce(Val)$_3$/TTIP proportion shows a minor increase of photoluminescence emissions with the small incorporations of Ce atom according with a decrease of "*a*" and an increment of "*c*" lattice parameters in anatase unit cell; **figure 6 of the manuscript**. At the Ce / Ti molar ratio $\geq 6 \times 10^{-3}$ there was a drastic reduction of both apical and equatorial Ti-O and O-O distances; shared and unshared O-O lengths are also condensed. From DRX analysis and Ti-O and O-O crystalline distances evaluation, it was determined that dopant presence caused the reduction of anatase unit cell along crystallographic *c* axis, due to the accommodation of Ce atom between occupied TiO6 octahedra. This location would markedly affect the Raman vibrational bands B1g(1), B1g(2) and A1g that corresponds to Ti and O vibration along "*c*" axis direction. We supposed that this distortion of anatase unit cell is also the cause of the decrease of photoluminescent band intensity.
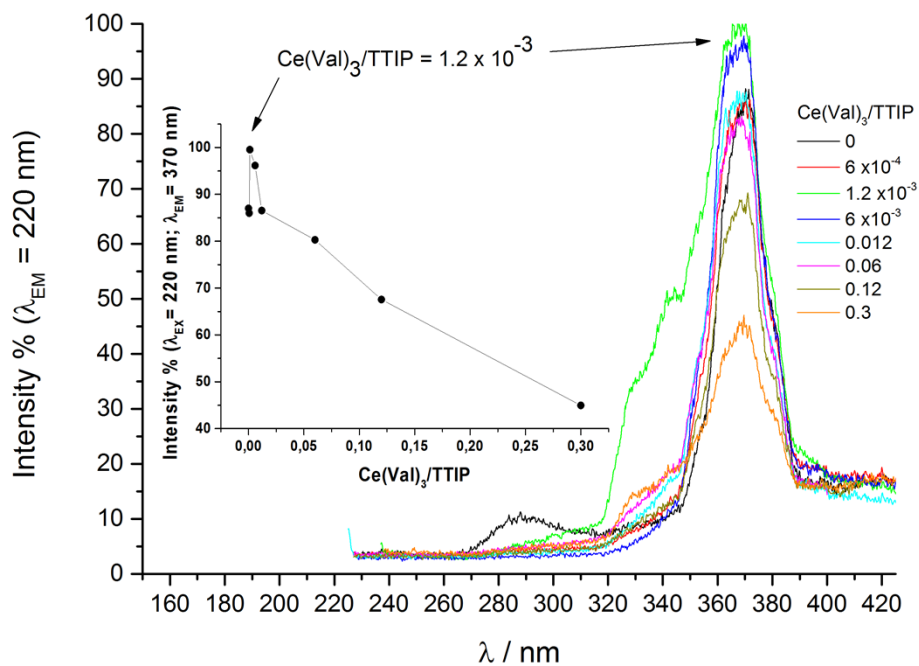
ESI 13. Photoluminescence (PL) emission spectra of Ce-anatase doped materials, λ_{EX} = 220 nm.

Inset: variation of photoluminescence band (λ_{EM} =370 nm) intensity against Ce(Val)$_3$/TTIP.

Citotoxicity tests:

Commercial anatase

Commercial anatase particles have an average size of about 20-150 nm
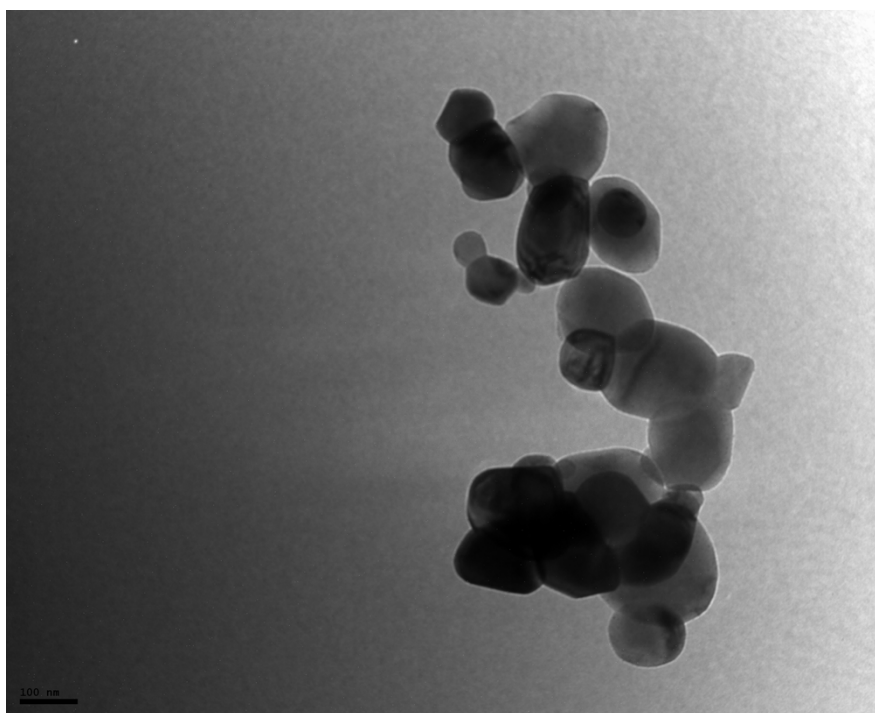
ESI14. TEM microphotograph of commercial anatase

Effect of the materials presence on Human Lung Epithelial cells (A549) growth
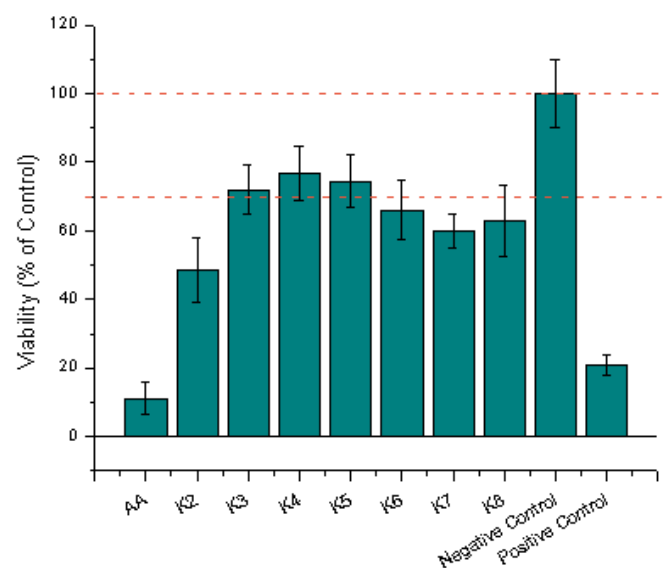
ESI15. A549 Cell viability

Material internalization on Human Lung Epithelial cells (A549). Cells can be distinguish as bright spots and dispersed particles as black dots. At t = 0 h, the material is dispersed among the epithelial cells. After 24h of contact it can be seen that the cells internalize the material. Similar results can be appreciated for all tested samples and for material-fibroblast interactions.
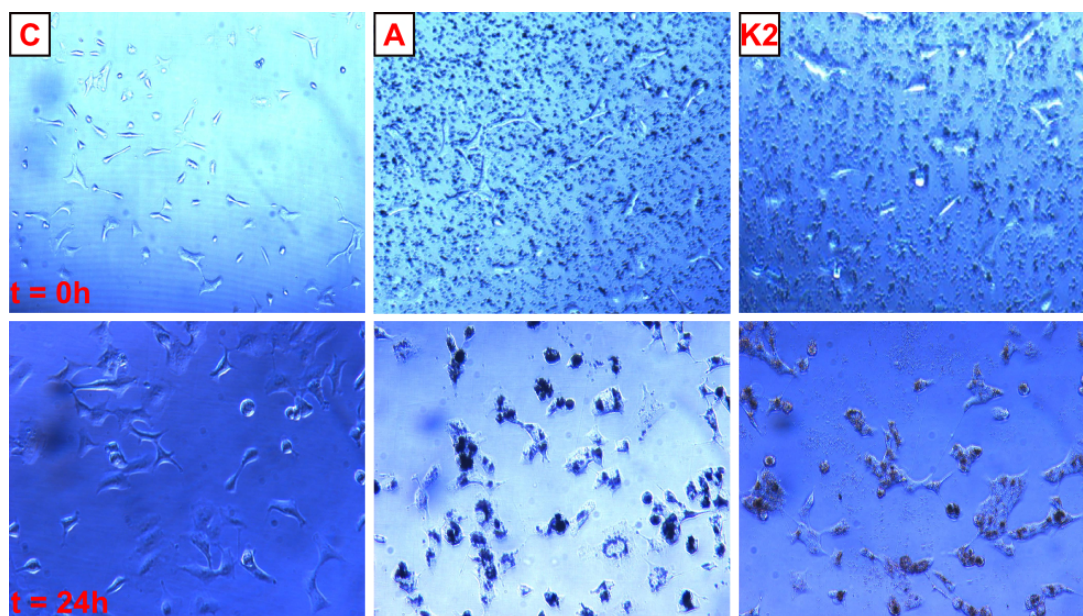
ESI16. Representative photographs of A549 cell interaction with the synthesized materials. C: Negative control; A: Commercial anatase; K2: 6.0×10^{-4} Ce(Val)$_3$/ TTIP molar ratio fullerene-like material.

References:

1. X. Wang and Y. Li, *Angew. Chem. Int. Ed.*, 2003, **42**, 3497-3500 and references therein.
2. N. Hassan, V. Verdinelli, J. M. Ruso and P. V. Messina, *Langmuir*, 2011, **27**, 8905-9812.
3. Messina P.V., Verdinelli V., Pieroni O. and Ruso J.M., *Colloid Polym Sci*, 2013, **291** 835-844 and references therein.
4. J. M. Ruso, A. N. Gravina, N. L. D'Elia and P. V. Messina, *Dalton Transactions*, 2013, **42**, 7991-8000.
5. A. N. Gravina, J. M. Ruso, J. A. Laiuppa, G. E. Santillan, J. L. Marco-Brown, N. L. D'Elia and P. V. Messina, *Journal of Materials Chemistry B*, 2014, **2**, 834-845.
6. B. E. Yoldas, *J. Mat. Sci.*, 1986, **21**, 1087-1092.
7. J.-K. Park, J.-J. Myoung, J.-B. Kyong and H.-K. Kim, *Bull. Korean Chem. Soc.*, 2003, **24** 671-673.
8. L. Qi, *Encycl. Surf. & Colloid Sci.*, 2006, 6183-6207 and references therein.
9. R. Tenne, L. Margulis, M. Genut and G. Hodes, *Nature*, 1992, **360**, 444-446.
10. J. C. Taylor, ed., *Rietveld made easy: a practical guide to the understanding of the method and successful phase quantifications*, Canberra: Sietronics Pty Ltd, 2001.
11. R. A. Young, ed., *The Rietveld Method*, 1993.
12. J. M. Ruso, V. Verdinelli, N. Hassan, O. Pieroni and P. V. Messina, *Langmuir*, 2013, **29**, 2350-2358.